Nondestructive Monitoring of a Multilayer Pressure Vessel: Strain Gages Instrumentation

Geraldo Cesar Rosario de Oliveira[1] ; Antonio dos Reis de Faria Neto[2] ; Erick Siqueira Guidi[3] ; Erica Ximenes Dias[4] ; Thais Santos Castro[5] ; Francisco José Grandinetti[6] ; Marcelo Sampaio Martins[7]

[1, 2, 3, 4, 5, 6, 7] *Department of Mechanical Engineering, São Paulo State University (UNESP), School of Engineering and Sciences, Guaratinguetá, Brazil,* geraldo.cesar@unesp.br, antonio.faria@unesp.br, erick.s.guidi@unesp.br, erica.ximenes@unesp.br, thais.castro@unesp.br, fj.grandinetti@unesp.br, *sampaio.martins@unesp.br*

Abstract– This article presents a method that allows verifying the safety of the operation of multilayer pressure vessels when inspection using ultrasonic testing equipment - an action commonly known as Non-Destructive Testing (NDT) - is not possible. In this context, strain gages were used to obtain strain values of the material related to stresses to which it is subjected by means of a pressurizing test. Once geometric characteristics and mechanical properties of the pressure vessel under study were known, it was possible to apply mechanics of materials concepts and obtain the biaxial state of principal stresses, thus inferring the actual thickness value of the accumulator. Moreover, it was possible to verify that although the use of strain gages takes longer than the ultrasound test, its degree of precision is remarkable and its applicability much wider, since geometric factors are not particularly concerning the shrinkage which occurs between the vessel layers. The data were also evaluated analytically and using finite element simulation, which demonstrated consistency with the results obtained by extensometry.

Keywords—Extensometry; Finite Elements; Thick Wall; Pressure Vessel; Instrumentation.

I. Introduction

The development of industries has required the use of high pressure lines and high pressure storage accumulators, as a result creating difficulties in assembling such equipment. In this context, multilayer pressure vessels are much easier to be assembled and the generated preload stress in the process of wrapping and clamping, on the other hand, redistributes stresses and allow the pressure vessel endure higher pressure [1]. It was commonly used from the 1960's to 1990's. Consequently, many multilayer pressure vessels have been in operation for about forty years. They have been submitted to different operating environments that change structural parameters and lead to subsequent problems in operation, which are becoming major concerns [2]. The American Society of Mechanical Engineers (ASME) [3], establish the rules concerning tolerance and dimensions, however, fatigue damage from years of operation must also be considered.

When there are not many pressurizing and depressurizing cycles during its operation, for example, characterizing low-cycle operation, fatigue is not the main problem [2, 4, 5]. However, monitoring the corrosion damage in pressure vessels using nondestructive evaluation (NDE) methods is rather usual, even though the equipment operates for several years and inspect structural modification at a given frequency is important, since most failures in operations are caused by corrosion. It is well-known that there is no ideal or suitable means of corrosion detection for all corrosion mechanisms [6 -

8]. In the context of pressure vessels, geometry, access (inspection nozzle) and placement are limiting factors to usual methods [9].

Short-ranging ultrasonic tests enables detection and evaluation of defects [10] based on the principles of geometrical acoustics and physical interaction of acoustic waves with the material and its defects [11, 12]. However, in a multilayer pressure vessel, contact between the outer and the inner layer deflects the wave, thus it is only possible to determine the thickness of each layer at a time through this method. The non-existence of an inspection nozzle that enables internal inspection is a hindrance to such an efficient method [9].

Strain gages allow indirect measurement in such a way that each gage consists in a fine metal grid that is stretched or shortened when the object is strained at the point to which the gage is attached [13]. By considering that the material under analysis is homogeneous, linearly elastic, isotropic and undergoes small deformations [14], it is possible to correlate the average strain of each filament submitted to the applied voltage with deformation and, consequently, with stress [15].

An NDE was performed on a hydraulic system component to apply similar pressure energy to a fluid in the path to service an open forging press for large steel parts the generated preload stress, whose capacity is 8.000 tons. In conjunction with a pump, the operation accumulator allows intermittent operation of the pump, and the presence of a control pressure vessel to homogenize the pressurized fluid, so that the accumulated energy is available to the operator, decreases pressure time. For such a purpose, it is necessary that the fluid, for example, compressed air, reaches pressure of 320 bar so that it can be characterized as a high pressure accumulator.

In this context, this work aims to perform measurements of the specific external deformations in the side and top of a pressure vessel. Calculate the principal stresses and compare them with the theoretical stresses. In addition, a computational simulation, using finite elements, will be performed to compare the obtained values.

II. METHODS

A. Assortment of instrumentation points

To carry out the NDE on strain gages, it is necessary to consider characteristics and properties of the equipment provided in Table 1. Once specific deformation is measured as

regards the linear proceeding of steel, the only remaining step is to find a theoretical approach that best suits the study case. Multilayer pressure vessels have a typical configuration in the manufacturing process, for example, each layer is between a contact pressure as shown in [16]. As it was not considered while the project was being carried out, a safer approach suggests treating the vessel as if there was no contact pressure, made by a perfect fit. In view of this, the analysis made deal with the mechanical behavior according to considerations for a thick-walled pressure vessel [16], as shown in Figure 1.

TABLE I
MECHANICAL AND GEOMETRICAL PROPERTIES OF THE PRESSURE VESSEL.

| Name	Symbol	Value
Elastics Modulus	E	200000 [MPa]
Poisson's Ratio	ν	0.30
Inner Vessel Radius	a	477.5 [mm]
Outer Vessel Radius	b	514.0 [mm]
Outer Sleeve Radius	c	553,95 [mm]
Inner Spherical Head Radius	a1	483.0 [mm]
Outer Spherical Head Radius	b1	541.5 [mm]
Operation Pressure	OP	31.38 [MPa]
Hydrostatic Test Pressure	HP	47.07 [MPa]
Fabrication Year	1978	
Fabricator	Hitachi Co. Ltda	
Operation Temperature	100	[°C]
Radiography	100	[%]
Project Code	Japaniese High Press. Gas Control Law	
Head Material	Jis G3115 SPV-36	
Shell Material	Jis G3115 SPV-50	
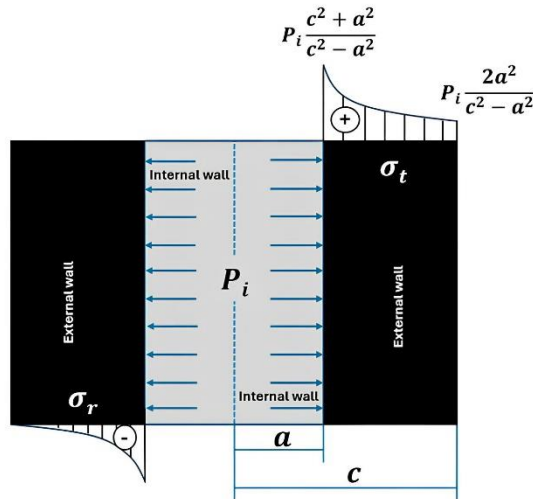
Fig. 1 Distribution of tangential and radial stresses in thick-walled tubes.

B. Assortment of instrumentation points

One of the most important issues in determining instrumentation points through strain gages is pressures applied on the chosen site. Nozzles and welds generate bending stresses which are undesirable given the required analytical approach [17]. For such a purpose, the points represented in Figure 2 were selected based on optimal and practical feasibility of access in order to ensure that A and B were free of bending stresses, so that there was no mutual interference whatsoever. C has two functions, since not only it allows the same analysis because the top is composed of a single layer, but its thickness is measured by ultrasound, thus allowing a comparison between a wider application of NDE and the proposed one [11, 18].
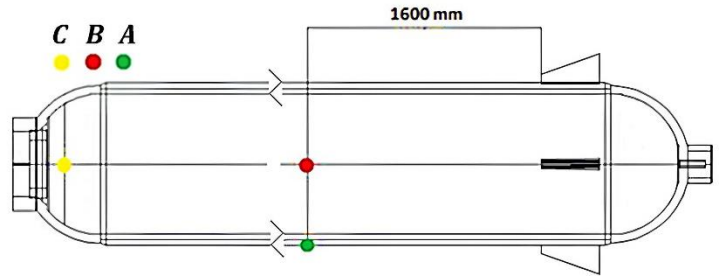
Fig. 2 Positioning of strain gauges in the pressure vessel.

C. Strain Gage Selection

To evaluate the evolution of deformations, the strain gage, in addition to being compatible with the analyzed material, must reflect a strain value related to a given side coordinate. As regards the triaxial state, XYZ, and terms how to calculate only the principal stress, both longitudinal and tangential, as shown in Equation (1), Equation (2) and Equation (3):

$$\sigma_t = \frac{p_i(c^2-a^2)}{(c^2-a^2)} \tag{1}$$

$$\sigma_t = \frac{2\,p_i a^2}{(c^2-a^2)} \tag{2}$$

$$\sigma_l = \frac{p\,a^2}{(c^2-a^2)} \tag{3}$$

Once the sensor is bonded in precise alignment with the main stresses, even more considering the work in the field, it is a task that almost impossible to be achieved. Fortunately, this problem can be circumvented by using rosettes, as it can be seen in Figures 3(a) – (c). These are a combination of three unidirectional gages offset from each other at a known angle. The chosen measurement grid is the one arranged at an angle of 45° - 120 Ω.

23ʳᵈ LACCEI International Multi-Conference for Engineering, Education, and Technology: "*Engineering, Artificial Intelligence, and Sustainable Technologies in service of society*". Hybrid Event, Mexico City, July 16 - 18, 2025

2

Fig. 3 Process of strain gauge bonding in pressure vessel where Figure (a) A point; Figure (b) B point and (c) C point.

Figure 2 shows the position of the rosettes on the side and top. The rosettes were positioned so that they were far from stress concentration points, so that experimental and theoretical values could be compared. The orientation of the strain gauges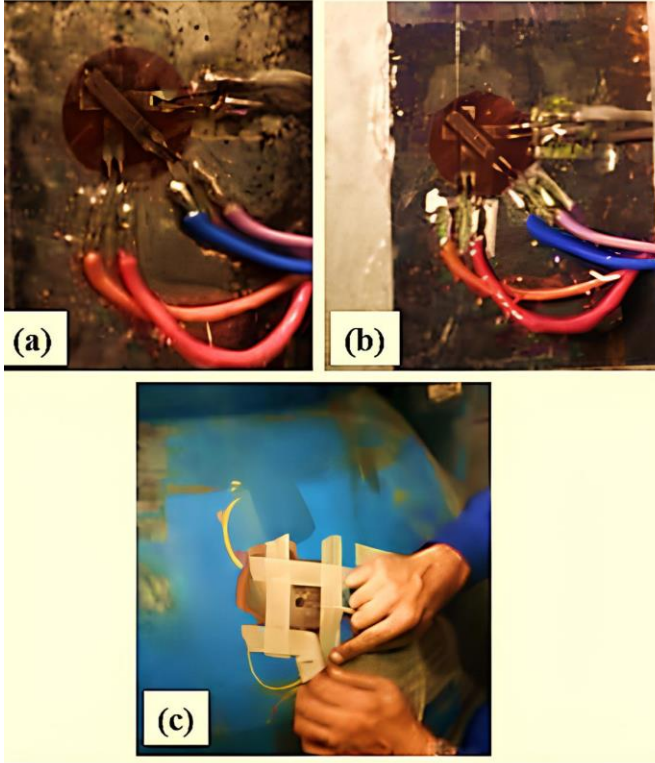 on each rosette in relation to the pressure vessel was: tangential (or circumferential), longitudinal and at 45° between them, as shown in the figure. To obtain the specific deformation data, the electrical strain gage technique was used, which consists of gluing electrical resistance strain gauges to a properly prepared surface. After applying the load, the strain gauge follows the deformations of the point on the surface where it is glued, varying its electrical resistance. The deformation to be measured is proportional to the variation in its electrical resistance.

Three rectangular rosettes (45°) were glued to three points (Figure 3) on the pressure vessel: two points located on the side and one point on the top. The strain gauges were connected to an electrical circuit in a ¼ Wheatstone bridge configuration, which, when connected to the HBM Quantum MX 1615 signal conditioner, provided the specific deformation values as the pressure vessel was pressurized. The electrical signal from the pressure transducer was also connected to the signal conditioner. Subsequently, deformation data were collected at the three points during the depressurization stage. The pressurization procedure was performed over a time interval of approximately 19 hours, while the depressurization procedure was performed over a time interval of approximately 5 hours.

D. Data Collection

After being assembled, the pressure vessel, pressurized at 29.42 MPa (300 kgf/cm²) was depressurized, which was chosen to represent the most critical operating conditions. In this process, the signal conditioner provided the ratio between the pressure value obtained by a transducer and deformation values, three for each respective point at the following coordinates: 0 °, 45 °, 90 °. The relations represented in Equations (4) and (5) enabled the determination of the related stress based on the properties described in Table 1.

$$\sigma_{0°} = \frac{E}{(1-\nu^2)}\left(\varepsilon_{0°} + \nu\varepsilon_{90°}\right)$$
$$(4)$$
$$\sigma_{90°} = \frac{E}{(1-\nu^2)}\left(\varepsilon_{90°} + \nu\varepsilon_{0°}\right)$$
$$(5)$$

However, these stresses directly related to these deformations do not represent the principal stress which can be explained by the theory of thick-walled pressure vessels. As the used strain gages were rosettes and angles between the data were collected, three deformations can be related through Equations (6) and (7), thus obtaining the principal stresses.

$$\sigma_1 = E\left[\frac{\varepsilon_{90°}+\varepsilon_{0°}}{2(1-\nu)} + \frac{1}{2(1+\nu)}\sqrt{(\varepsilon_{90°}-\varepsilon_{0°})^2 + (2\varepsilon_{45°}-\varepsilon_{0°}-\varepsilon_{90°})^2}\right] \quad (6)$$

$$\sigma_2 = E\left[\frac{\varepsilon_{90°}+\varepsilon_{0°}}{2(1-\nu)} - \frac{1}{2(1+\nu)}\sqrt{(\varepsilon_{90°}-\varepsilon_{0°})^2 + (2\varepsilon_{45°}-\varepsilon_{0°}-\varepsilon_{90°})^2}\right] \quad (7)$$

III. RESULTS AND DISCUSSION

A. Experimental specific deformations at points A, B and C during pressurization.

Table 2 shows the experimental results at points A, B and C according to the equipment reading. In this table, there is:

ε_{AL} – Specific deformation at point A, in the longitudinal direction;
εA_{45} – Specific deformation at point A, at 45° in relation to the longitudinal direction;
ε_{AT} – Specific deformation at point A, in the tangential direction.
ε_{BL} – Specific deformation at point B, in the longitudinal direction;
εB_{45} – Specific deformation at point B, at 45° in relation to the longitudinal direction;
ε_{BT} – Specific deformation at point B, in the tangential direction.

23rd LACCEI International Multi-Conference for Engineering, Education, and Technology: "*Engineering, Artificial Intelligence, and Sustainable Technologies in service of society*". Hybrid Event, Mexico City, July 16 - 18, 2025

3

ε_{CL} – Specific deformation at point C, in the longitudinal direction;

ε_{C45} – Specific deformation at point C, at 45° in relation to the longitudinal direction;

ε_{CT} – Specific deformation at point C, in the tangential direction.

TABLE II
SPECIFIC DEFORMATIONS MEASURED AT POINTS A, B AND C

Pressure (MPa)	ε_{AL} (μm/m)	ε_{A45} (μm/m)	ε_{AT} (μm/m)	ε_{BL} (μm/m)	ε_{B45} (μm/m)
20.900	149.388	297.480	444.271	114.894	286.170
21.100	155.985	309.760	455.245	120.384	298.160
22.000	173.389	330.930	488.798	136.253	319.780
23.100	185.962	356.540	520.041	153.014	342.230
24.100	205.164	383.790	554.081	171.727	369.330
25.100	223.651	412.980	588.982	190.595	395.410
26.000	242.368	439.040	621.439	209.605	420.840
27.000	258.978	463.030	651.668	225.313	443.940
28.000	278.217	492.530	687.796	245.410	472.780
28.900	293.896	515.090	716.893	260.065	494.440
29.700	307.808	537.840	744.629	276.152	516.470

Pressure (MPa)	ε_{BT} (μm/m)	ε_{CL} (μm/m)	ε_{C45} (μm/m)	ε_{CT} (μm/m)
20.900	474.581	160.799	155.191	156.730
21.100	483.675	166.673	160.831	162.566
22.000	516.027	199.496	193.396	195.516
23.100	549.016	237.303	231.447	233.201
24.100	584.513	271.192	264.503	267.101
25.100	620.316	313.491	306.610	308.157
26.000	653.377	348.153	341.175	342.694
27.000	685.427	380.003	372.756	374.066
28.000	727.204	414.800	408.346	409.189
28.900	753.283	440.584	432.964	434.087
29.700	782.508	475.140	467.047	468.222

With the measured values (Table 2), the experimental stresses at point A and in the longitudinal and tangential directions were obtained through Equations (4) and (5). For points B and C, similar expressions were used. Table 3 shows

the results of the experimental normal stresses at points A, B and C and the subscript e, refers to experimental results, L, longitudinal and T, tangential.

B. Experimental normal stresses at points A, B and C during pressurization

TABLE III
EXPERIMENTAL STRESSES AT POINTS A, B AND C

Pressure (MPa)	σ_{ALe} MPa	σ_{ATe} MPa	σ_{BLe} MPa	σ_{BTe} MPa	σ_{CLe} MPa	σ_{CTe} MPa
20.900	62.125	107.492	56.542	111.879	45.674	45.048
21.100	64.299	110.339	58.349	114.240	47.350	46.718
22.000	70.336	118.860	63.969	122.396	56.736	56.124
23.100	75.159	126.556	69.828	130.752	67.530	66.899
24.100	81.624	135.303	76.282	139.787	77.214	76.584
25.100	87.988	144.193	82.789	148.900	89.217	88.397
26.000	94.242	152.560	89.147	157.419	99.112	98.273
27.000	99.885	160.299	94.712	165.499	108.181	107.267
28.000	106.496	169.508	101.884	176.006	118.144	117.281
28.900	111.860	176.937	106.824	182.704	125.453	124.453
29.700	116.747	183.950	112.287	190.188	135.298	134.234

C. Experimental principal stresses at points A, B and C during pressurization.

The principal stresses at points A, B and C were calculated using the equations obtained from the analysis of the rectangular rosette, Equation (6) and (7). They are shown in Table 4.

TABLE IV
EXPERIMENTAL PRINCIPAL STRESSES AT POINTS A, B AND C

Pressure (MPa)	σ_{A1e} MPa	σ_{A2e} MPa	σ_{B1e} MPa	σ_{B2e} MPa	σ_{C1e} MPa	σ_{C2e} MPa
20.900	107.492	62.125	111.910	56.511	45.994	44.729
21.100	110.347	64.290	114.246	58.342	47.697	46.371
22.000	118.860	70.336	122.413	63.953	57.133	55.728
23.100	126.562	75.153	130.782	69.798	67.880	66.550
24.100	135.311	81.616	139.816	76.253	77.680	76.118
25.100	144.212	87.969	148.936	82.753	89.574	88.040

23rd LACCEI International Multi-Conference for Engineering, Education, and Technology: "*Engineering, Artificial Intelligence, and Sustainable Technologies in service of society*". Hybrid Event, Mexico City, July 16 - 18, 2025

4

26.000	152.581	94.221	157.459	89.108	99.469	97.916
27.000	160.322	99.862	165.543	94.669	108.525	106.923
28.000	169.542	106.462	176.064	101.825	118.421	117.005
28.900	176.971	111.826	182.751	106.777	125.791	124.115
29.700	183.997	116.699	190.238	112.236	135.656	133.876

It can be observed that the values found for the principal stresses are very close to the values of the longitudinal and tangential stresses for points A, B and C, proving that the longitudinal and tangential classifications are already the main ones.

D. *Experimental specific deformations at points A, B and C during depressurization and the respective tensions of interest*

Now, the main stresses for depressurization are presented, Table 5. The method used is identical to that used in pressurization, with the results shown above, in Table 2.

TABLE V
SPECIFIC DEFORMATIONS MEASURED AT POINTS A, B AND C - DEPRESSURIZATION

Pressure* (MPa)	ε_{AL*} (µm/m)	ε_{A45*} (µm/m)	ε_{AT*} (µm/m)	ε_{BL*} (µm/m)	ε_{B45*} (µm/m)
0.400	2.920	4.620	7.250	3.250	4.880
1.520	14.440	20.560	29.100	15.540	23.430
3.900	48.060	75.910	104.650	46.460	76.280
6.730	82.780	131.230	180.060	74.020	126.370
10.300	126.320	201.460	275.620	111.670	193.140
14.250	176.060	282.610	383.460	154.720	265.280
17.250	211.210	339.710	462.690	184.540	319.070
19.100	232.660	376.020	513.320	203.640	353.120
20.400	249.000	402.880	550.500	215.320	376.070
21.900	260.700	427.210	584.810	226.340	397.270
22.900	267.530	442.000	606.640	231.770	410.810
28.500	325.270	544.320	747.710	278.770	497.870

Pressure* (MPa)	ε_{BT*} (µm/m)	ε_{CL*} (µm/m)	ε_{C45*} (µm/m)	ε_{CT*} (µm/m)
0.400	7.670	2.610	2.480	2.540
1.520	32.860	12.160	11.650	12.020
3.900	112.680	53.890	51.270	49.210
6.730	188.310	90.690	85.130	80.630

10.300	285.980	138.670	130.670	123.180
14.250	395.230	201.990	191.740	180.970
17.250	474.030	239.920	228.530	215.750
19.100	525.890	266.750	255.080	241.620
20.400	560.940	286.830	275.160	262.270
21.900	596.340	302.570	292.130	279.880
22.900	618.090	319.850	309.630	297.740
28.500	758.710	404.630	397.190	387.490

Once the deformations at points A, B and C have been obtained, the normal stresses and principal stresses for depressurization can be calculated in the same way as was done for pressurization. As shown in Tables 6 and 7, respectively.

TABLE VI
EXPERIMENTAL STRESSES AT POINTS A, B AND C - DESPRESSURIZATION

Pressure (MPa)	σALe* MPa	σATe* MPa	σBLe* MPa	σBTe* MPa	σCLe* MPa	σCTe* MPa
0.400	1.120	1.786	1.220	1.900	0.741	0.730
1.520	5.092	7.348	5.582	8.247	3.465	3.444
3.900	17.463	26.169	17.640	27.828	15.089	14.369
6.730	30.065	45.032	28.684	46.267	25.248	23.700
10.300	45.935	68.905	43.399	70.216	38.599	36.216
14.250	63.978	95.885	60.064	97.065	56.325	53.092
17.250	76.927	115.616	71.813	116.350	66.955	63.236
19.100	84.979	128.158	79.430	129.007	74.557	70.691
20.400	91.022	137.407	84.308	137.480	80.332	76.554
21.900	95.856	145.719	89.064	145.987	84.953	81.462
22.900	98.796	150.967	91.692	151.125	89.928	86.526
28.500	120.787	185.778	111.293	185.130	114.478	111.842

TABLE VII
EXPERIMENTAL PRINCIPAL STRESSES AT POINTS A, B AND C- DESPRESSURIZATION

Pressure* (MPa)	σA1e* MPa	σA2e* MPa	σB1e* MPa	σB2e* MPa	σC1e* MPa	σC2e* MPa
0.400	1.794	1.112	1.912	1.208	0.751	0.720
1.520	7.363	5.077	8.252	5.577	3.523	3.386
3.900	26.169	17.462	27.853	17.615	15.091	14.366
6.730	45.032	30.065	46.298	28.653	25.252	23.696
10.300	68.905	45.935	70.244	43.370	38.599	36.215
14.250	95.891	63.972	97.125	60.003	56.326	53.091
17.250	115.621	76.922	116.405	71.758	66.958	63.233
19.100	128.163	84.974	129.072	79.365	74.562	70.686
20.400	137.412	91.017	137.545	84.243	80.334	76.551
21.900	145.728	95.846	146.069	88.982	84.958	81.456
22.900	150.978	98.785	151.205	91.612	89.933	86.522
28.500	185.801	120.765	185.269	111.154	114.490	111.830

E. *Theoretical stresses at points A, B and C*

To obtain the theoretical stresses, the thick-walled tube theory was used, since the ratio between the tube thickness and the internal radius is greater than 10%. In this case, the tangential and radial stresses behave as shown in Figure 1. On

23rd LACCEI International Multi-Conference for Engineering, Education, and Technology: "*Engineering, Artificial Intelligence, and Sustainable Technologies in service of society*". Hybrid Event, Mexico City, July 16 - 18, 2025

5

the internal surface there is a triple stress state (longitudinal, radial and tangential stress), while on the external surface there is a biaxial state (longitudinal and tangential stress).

The tangential and radial stresses in the side are given by:

- On the internal surface, the tangential stress is equivalent to Equation (1) and the radial stress has a value equal to pi, where pi is the internal pressure;
- On the outer surface, the tangential stress is equivalent to Equation (2) and the radial stress has a value equal to zero;
- Longitudinal stresses are obtained considering uniform stress distribution, according to Equation (3).
- In the spherical top, the tangential stresses were obtained by the thin-wall theory, Equation (8):

$$\sigma_t = \frac{p_i a_1}{2t}$$
(8)

Table 8 shows the tangential and longitudinal stresses calculated according to the theoretical expressions above.

TABLE VIII
THEORICAL PRINCIPAL STRESSES AT POINTS A, B AND C

Pressure (MPa)	σ_{ALt} MPa	σ_{ATt} MPa	σ_{BLt} MPa	σ_{BTt} MPa	σ_{CLt} MPa	σ_{CTt} MPa
0.000	0.000	0.000	0.000	0.000	0.000	0.000
2.000	5.783	11.566	5.783	11.566	8.254	8.254
4.000	11.566	23.132	11.566	23.132	16.507	16.507
6.000	17.349	34.698	17.349	34.698	24.761	24.761
8.000	23.132	46.264	23.132	46.264	33.014	33.014
10.000	28.915	57.830	28.915	57.830	41.268	41.268
12.000	34.98	69.396	34.698	69.396	49.522	49.522
14.000	40.481	80.962	40.481	80.962	57.775	57.775
16.000	46.264	92.528	46.264	92.528	66.029	66.029
18.000	52.047	104.093	52.047	104.093	74.282	74.282
20.000	57.830	115.659	57.830	115.659	82.536	82.536
22.000	63.613	127.225	63.613	127.225	90.789	90.789
24.000	69.396	138.791	69.396	138.791	99.043	99.043
26.000	75.179	150.357	75.179	150.357	107.297	107.297
28.000	80.962	161.923	80.962	161.923	115.550	115.550
30.000	86.745	173.489	86.745	173.489	123.804	123.804

Once the main stress was determined according to the data obtained by the strain gages analyses and Equations (6) and (7), similar values at points A and B were verified, thus the instrumentation was validated as successful. At Point C, values were identical, which is typical of spherical geometry. In Figure 4, the experimental values can be compared with those obtained from Equations (2) and (3) as for the pressure variation in the test.
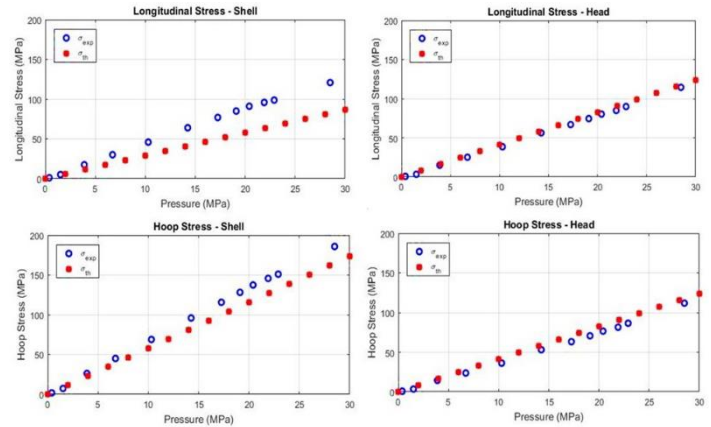

Fig. 4 Tangential and longitudinal stresses at points A and C. (At point B, stresses similar to those at point A act) – despressurization

The experimental linearity and similarity between the two analyzes allow inferring an indirect relation for safety inspection of the pressure vessel. To estimate the side thickness, Equation (2) was used, which equates the values of experimental tangential stress obtained from the depressurization test. Therefore, the value to be obtained from this equation will be the internal radius by considering that the external radius, in addition to being measured, must be subjected throughout operating time so that a very mild corrosion effect is produced. From this relation, once the internal radius (a) value is known, the external radius (c) is obtained.

When all pressures concerning the geometry of the pressure accumulator were analyzed, a minimum value of 33.9 mm of internal thickness was reached. With due consideration of design as regards safe working pressure conditions, experimental tangential stresses on the side and top (on the outer surface) corresponding to an internal pressure of 29.7 MPa are already close to the material stress value established by the JIS standard (SPV 355, with σ_{adm} = 160 MPa and SPV490, with σ_{adm} = 195 MPa). Furthermore, on the inner surface, tangential stresses are greater than on the outer surface (if there is no contact pressure between the vessels). Thus, according to experimental stresses, it is considered that pressure of 29.7 MPa is already on the recommended limit. The determined values can be compared with properties of pressure vessel materials show.

To complement the evaluation, a simulation was performed using the finite element tool, Figure 5, through the Inventor software. Finite elements are a powerful tool in engineering,

23rd LACCEI International Multi-Conference for Engineering, Education, and Technology: "*Engineering, Artificial Intelligence, and Sustainable Technologies in service of society***".** Hybrid Event, Mexico City, July 16 - 18, 2025

6

used in various fields, bringing together theory and practice through computational simulation [19 – 21]. With this, the principal stresses were obtained at the points studied and the coherence in terms of magnitude of the experimentally and theoretically obtained values was observed. This ratifies the method using extensometry to measure stresses in pressure vessels.
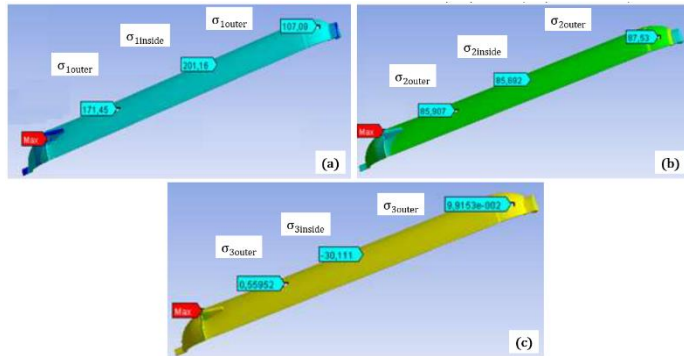

Fig. 5 Principal stresses determined by means of finite elements

According to [22], NDT techniques are essential for quality assessment and performance prediction. They are also used to locate damage and identify failure modes of pressure vessels. In this work, the use of NDT, specifically the application of extensometry, was essential to obtain the deformations and stresses generated in the pressure vessel when a load is applied. Furthermore, the use of FEM is common in the assessment of the structural integrity of pipelines and pressure vessels, due to its ability to model defects and predict stress loads. It is a tool that, together with other NDT techniques, enables the assessment of structures and monitoring in operation [22 – 25].

IV. Conclusions

From the analysis of the data obtained, it was observed that the measurements performed by means of extensometry presented results very close to those predicted by the theoretical equations, evidencing the reliability of this technique for monitoring stresses in multilayer pressure vessels. Furthermore, the application of the finite element method proved to be an effective and accurate tool in obtaining stress fields, reinforcing its relevance in structural analyses and in the development of engineering projects. In this way, the pressure vessel can be monitored and its safety in operation ensured. It is worth mentioning that for this case it was necessary to use the multilayer theory, a difficult case to be addressed in operation, demonstrating the applicability between theory and practice.

Acknowledgment

References

[1] Z. Liang, J. Nan, and L. Sijia, "Experimental study of integrated multilayer clamping high pressure vessel," *J. Press. Vessel Technol.,* vol. 133, no 6, pp. 61206 – 61212, December 2011.

[2] M. Zhao and R. Parkinson, "Risk-based operations assessment of a multilayered vessel under cyclic loading conditions," *J. Press. Vessel Technol.,* vol. 136, no 2, pp. 489-496, August 2013.

[3] ASME, "Boiler and Pressure Vessel Code", Section VIII, Division 1: Rules for Construction of Pressure Vessels, *American Society of Mechanical Engineers*, 2015.

[4] H. C. Sampaio, R. A. Dias and J. A. P. Balestieri, "Sustainable Urban Energy Planning: The Case Study of a Tropical City," *Appl. Energy*, vol. 104, pp. 924–935, April 2013.

[5] P. V. Piping and S. Eng, "Fatigue Abstracts," *Situ*, vol. 63, no 10, pp. 2–3, November 1995.

[6] A. R. Faria Neto, A. P. N. Souza, R. R. Passos, M. S. Pereira, L. A. Pocrifka, R. F. Brambilla Souza and E. Costa Rios, " Evaluation of Paullinia Cupana as a green corrosion inhibitor for carbon steel utilizing gravimetric and electrochemical noise techniques", *Materials Research Express*, vol. 6, no. 7, pp. 076522, April 2019.

[7] V. S. Agarwala, P. L Reed, S. Ahmad, "Corrosion detection and monitoring – A review", *Nace Corrosion* p. NACE-00271, 2000.

[8] E. Bardal and J. M. Drugli, "Corrosion detection and diagnosis", *Materials science and engineering*, vol. 3, pp. 144-164, 2004.

[9] M. G. Lozev, R. W. Smith and B. B. Grimmett, "Evaluation of Methods for Detecting and Monitoring of Corrosion Damage in Risers*," J. Press. Vessel Technol.*, vol. 127, no 3, pp. 244-254, August 2005.

[10] J. Prager, J. Kitze, C. Acheroy, D. Brackrock, G. Brekow and M. Kreutzbruck, "SAFT and TOFD - A Comparative Study of Two Defect Sizing Techniques on a Reactor Pressure Vessel Mock-Up," *J. Nondestruct. Eval.*, vol. **32, no** 1, pp. 1–13. August 2013.

[11] Neiss, G., "Nondestructive inspection of nozzle inner corner at boiling water reactor pressure vessels with ultrasound-flaw detection and crack depth determination," *Nucl. Engeneering Des.*, vol. 87, pp. 175–184, July 1985.

[12] K. H. Matlack, J. Y. Kim, J. J. Wall, J. Qu, L. J. Jacobs and M. A. Sokolov, "Sensitivity of Ultrasonic Nonlinearity to Irradiated, Annealed, and Re-Irradiated Microstructure Changes in RPV Steels," *J. Nucl. Mater.,* vol. **448, no** 1–3, pp. 26–32, May 2014.

[13] N. T. Younis and B. Kang, "Averaging Effects of a Strain Gage," *J. Mech. Sci. Technol.*, vol. **25, no.** 1, pp. 163–169. March 2011.

[14] H. Sarangi, K. S. R. K. Murthy and D. Chakraborty, "Optimum Strain Gage Locations for Accurate Determination of the Mixed Mode Stress Intensity Factors," *Eng. Fract. Mech.*, vol. 88, pp. 63–78, July 2012.

[15] C. Carral, N. Charvin, H. Trouvé and P. Mélé, "An Experimental Analysis of PEMFC Stack Assembly Using Strain Gage Sensors," *Int. J. Hydrogen Energy*, vol. 39, no 9, pp. 4493–4501, March 2014.

[16] V. Féodossiev, *Tubos de paredes gruesas y discos*. In: P. G. Mora, *Résistance Des Matériaux,* Éditions de la Paix, pp. 301 – 305, 1980.

[17] S. Marlette, P. Freyer, M. Smith, A. Goodfellow, X. Pitoiset, B. Voigt, R. Rishel, and E. Kingston, "Simulation and Measurement of Through–Wall Residual Stresses in a Structural Weld Overlaid Pressurizer Nozzle," *J. Press. Vessel Technol.*, vol. 136, no 5, pp. 1425-   1433, January 2011.

[18] B. H. Chance and D. E. Bray, "Nondestructive Monitoring of Stress Relaxation in Welded Steel Plates," *J. Press. Vessel Technol.*, vol. 124, no 3, pp. 343-348, July 2002.

[19] F. C. S. De Almeida, G. C. R. Oliveira and E. S. Guidi, "Study of the Stress Concentration Factor in PPS/C Type Composite Using FEA and Analytical Method," *SAE Technical Paper*, no 2024-36-0072, 2024.

[20] C. S. S. Rigo, A. D. R. D. F. Neto, F. J. Grandinetti, T. S. Castro, E. X. Dias, and M. S. Martins, "Development of the Steering System for a Formula SAE Prototype," *SAE Technical Paper*, no 2024-36-0099, 2024.

[21] L. O. Gomes, F. J. Grandinetti, M. S. Martins, A. M. Soares, A. R. de Faria Neto, T. S. Castro and L. F. Almeida, "Brake Pedal Sizing and

23rd LACCEI International Multi-Conference for Engineering, Education, and Technology: "*Engineering, Artificial Intelligence, and Sustainable Technologies in service of society*". Hybrid Event, Mexico City, July 16 - 18, 2025

7

Preliminary Design of Balance Bar in the Brake of a SAE Formula Type Vehicle," *SAE Technical Paper*, no 2024-36-0054, 2024.

[22]   W. Zhou, J. Wang, Z. Pan, J. Liu, L. Ma, J. Zhou, Y. Su, "Review on optimization design, failure analysis and non-destructive testing of composite hydrogen storage vessel", *International journal of hydrogen energy*, vol. 47, no. 91, pp. 38862-38883, november 2022.

[23]   S. D. Vijaya Kumar, M. Lo Yin Kai, T. Arumugam, S. Karuppanan, "A review of finite element analysis and artificial neural networks as failure pressure prediction tools for corroded pipelines", *Materials*, vol. 14, no. 20, pp. 6135, october 2021.

[24]   G. C. R. d. Oliveira, V. A. Rosario de Oliveira, C. A. Alvarado Silva, E. S. Guidi and F. d. A. Silva, "Modeling the Stress Field in MSLA-Fabricated Photosensitive Resin Components: A Combined Experimental and Numerical Approach." *Modelling*, vol 6, no 3, january 2025.

[25]   C. A. Alvarado Silva, , A. C. De Souza, G. C. R. de Oliveira, F. Azevedo Silva, B. U. Rubio, "Experimental Analysis of the Failure of the Bearing Support of a Cardan Shaft | Análise Experimental da Falha do Suporte de Mancal de um Eixo Cardan", *Proceedings of the LACCEI international Multi-conference for Engineering, Education and Technology*, july 2022.

23rd LACCEI International Multi-Conference for Engineering, Education, and Technology: "*Engineering, Artificial Intelligence, and Sustainable Technologies in service of society***".** Hybrid Event, Mexico City, July 16 - 18, 2025

8